



An inclusive numerical framework to assess the role of feedstock features on the quality of cold spray deposits

A. Ardeshiri Lordejani, D. Colzani, M. Guagliano, S. Bagherifard*

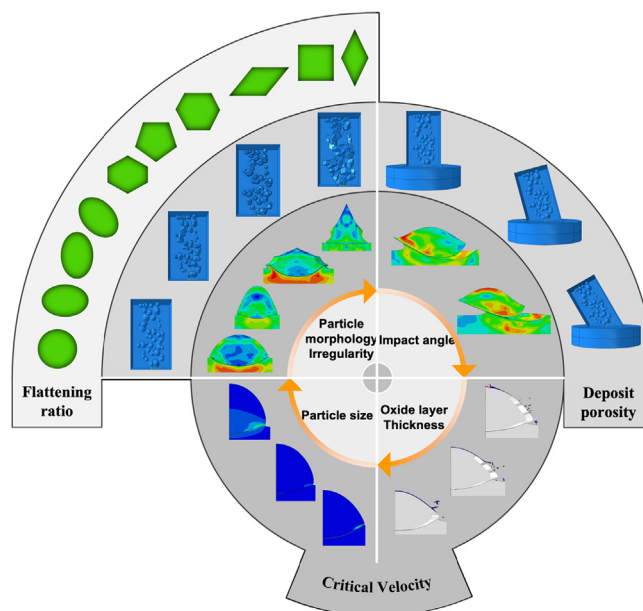
Department of Mechanical Engineering, Politecnico di Milano, Milano, Italy



HIGHLIGHTS

- An inclusive numerical framework is developed to assess the role of feedstock features (size, morphology, oxidation extent and impact angle) on cold spray deposit quality.
- The efficiency of multiple FEM approaches including Lagrangian, smoothed particle hydrodynamics (SPH), and coupled Eulerian-Lagrangian is evaluated.
- Deposit quality indicators involving critical velocity, particle flattening, and porosity have been assessed as a function of each powder feature.
- Comparison with experimental data confirmed the capacity of the proposed framework to tune the deposit properties as a function of a wide range of primary and secondary powder characteristics.

GRAPHICAL ABSTRACT



ARTICLE INFO

Article history:

Received 1 July 2022

Revised 8 November 2022

Accepted 11 November 2022

Available online 14 November 2022

Keywords:

Supersonic deposition
Finite element method
Coating
Additive manufacturing
Powder

ABSTRACT

Cold spray technology provides unique capabilities for coating, repair, and additive manufacturing. However experimental trial and error to optimize deposit quality indexes, that rely on powder characteristics, can be costly and tedious. In this research, multiple finite element modelling approaches were compared regarding their capability and shortcomings to analyze the role of major powder features on deposit properties. Lagrangian and CEL methods were selected as the most robust approaches for analyzing the single/multi-particle impact condition, respectively. An intricate algorithm was introduced to accurately evaluate the effect of parameters including particle size, shape, oxidation extent, and impact angle on the deposition indicators such as critical velocity, particle flattening, and deposit porosity. The results exhibited a good agreement with the reported experimental data, confirming the capacity of the proposed numerical framework to tune the deposit properties as a function of a wide range of feedstock characteristics. It was concluded that for successful deposition, the effect of various powder properties and their respective effect and contribution towards plastic deformation should be taken into account. The results indicated that for a given particle velocity, smaller particle, more irregular morphology,

* Corresponding author.

E-mail address: sara.bagherifard@polimi.it (S. Bagherifard).

thicker oxide layer, and smaller impact angle will result in limited particle deformation and a lower possibility of successful adhesion.

© 2022 The Authors. Published by Elsevier Ltd. This is an open access article under the CC BY-NC-ND license (<http://creativecommons.org/licenses/by-nc-nd/4.0/>).

1. Introduction

Cold spray (CS) sets itself apart from other thermal spraying processes for the lower working temperature, which is compensated by higher particle velocity. In CS, particles accelerated to supersonic velocities, impact and adhere to the substrate through mechanisms, which are proposed to be associated with adiabatic shear instability, among other possible phenomena [1,2]. Throughout the CS process, unlike other thermal spraying methods, severe oxidation, recrystallization, and phase change due to thermal effects are absent; this provides CS with unique advantages in different applications varying from surface coating to repair, surface functionalization, and more recently additive manufacturing [3]. The potential of CS for additive manufacturing of freeform objects has been verified and compared against other established additive manufacturing methods [4–6]. However, further development of CS additive manufacturing for structural applications poses a range of new challenges that encompass different aspects of the process [7]. Thus, gaining the ability to precisely assess the effect of various parameters on the efficiency of the process and the characteristics of the deposit have become even more crucial. The major process parameters in CS include carrier gas pressure and temperature, powder size distribution, shape and oxidation extent, substrate surface state, and nozzle stand-off distance, to name just a few. Assessing the interrelated effect of the mentioned parameters on the deposit quality requires a careful selection of the optimum values for the controllable variables. This can be done through rigorous and extensive experimental procedures that require a considerable time and cost dedication, thus, hindering further expansion of the CS process versatility. Indeed, for many powder-substrate material combinations, the optimum set of CS parameters are yet to be developed [8].

Simulating the deposition process at different scales can facilitate evaluating the effect of individual parameters on the deposit quality at a considerably reduced cost [9,10]. Finite element (FE) analysis is a powerful and comparably efficient tool to study the effect of process parameters on particle deformation, interaction, adhesion, and coating characteristics. However, the dynamic nature of the process, the high strain-rate plastic deformation, the complex thermo-mechanical interactions, and the consideration of adhesion mechanisms make it impossible to define a comprehensive model employing a single FEA formulation. The demanding nature of parameter selection in CS has driven the researchers to apply distinctive numerical simulation approaches for studying CS parameters. The simulation methods employed for CS modelling can be categorized into two groups of micro and macro-scale simulations, single particle impact model being considered as micro-scale simulation, and high number multi-particle impact as macro-scale. This is important since while there may be a connection between the trends observed in micro and macro-scale, the results may not be directly extendable.

Lagrangian approach is the most extensively employed FEA method, and as a result, numerous studies explore different aspects of CS using this approach [9–15]. While Lagrangian approach is susceptible to instabilities and convergence issues arising from high or rapid deformations, its ability to simulate discrete solid behavior and inter-boundary interactions make it a suitable method to study the main aspects of single particle impact. Lagrangian formulation has been utilized to study the splat's (deformed

particle's) form, flattening ratio, jetting, and estimation of critical velocity for single particle impact in CS [9,16].

Arbitrary Lagrangian-Eulerian (ALE) approach is a combination of Lagrangian and Eulerian formulations. In ALE, while the topology of the prior element structure is kept intact and the outer boundary of the mesh arrangement is constrained to move with the material, the inner mesh is allowed to move and resize independently. This feature can alleviate the convergence issues associated with large plastic deformations; however, it should be carefully adapted to avoid any numerical inaccuracies, such as unrealistic deformation or decrease in the equivalent plastic strain, which may be caused by mesh remapping in the presence of high plastic strain gradients at the interfacial regions [9,12,13,17].

Smoothed particle hydrodynamics (SPH) is a mesh-free FEA method, which does not require discretization into connected elements. Instead, the body is discretized into a collection of points, which are referred to as particles; the properties of each particle are interpolated based on the corresponding values of the adjacent particles. As a fully Lagrangian approach, SPH is suitable for problems involving fluid flow or large deformations as it can avoid the issues related to excessive element distortion [18]. However, it is limited by shortcomings in simulating tensile stresses, surface loads, and specific forms of contact [11,19–23].

Coupled Eulerian-Lagrangian (CEL) method offers the possibility to simulate the interaction between bodies with either Eulerian or Lagrangian formulation in the same model. This method takes advantage of the material free flow in the Eulerian domain to model severe deformation. This ability makes CEL a perfect candidate for analyzing the interaction between solid and fluid (or fluid-like) bodies [24–26].

In this research, we first reviewed and compared various FEA modelling approaches in terms of suitability for CS modeling and then developed different FEA schemes to simulate the effect of individual variables in single and multi-particle impact in CS, while accounting for particle-substrate adhesion. We utilized the developed models to critically investigate the effect of particle size, particle shape, oxide layer thickness and angle of impact on the key process indexes including particle critical velocity, deformation ratio, and deposit porosity. These specific set of parameters were considered due to their strong interrelation and their importance on the final properties of the deposit.

The ability of different modelling approaches in simulating the effect of individual feedstock parameter indicator was assessed and the models were validated against available experimental data. The effect of each considered variable was studied using the appropriate modelling technique, changing a single input at a time. When needed, new characterizing indexes were proposed to elucidate the role of powder characteristics on the deposit quality. This study offers a holistic numerical framework to investigate the effect of a wide range of primary and secondary powder parameters on CS deposit's quality, at a high accuracy and considerably reduced cost and can steer further studies in the field towards the right direction.

2. Comparison of different modelling approaches

For an overall comparison, Lagrangian and ALE methods are the most extensively studied approaches for simulation of CS single particle impact [12,27]. The distinct boundary definition and

flexibility in considering different interaction properties make them advantageous to assess the effects of various process parameters. CEL approach, instead, can be considered as the most suitable technique for simulation of multi-particle impact, which also offers flexibility for considering multi-material feedstock [28]. Although SPH method has not been so far used for a case with multi-material powder mixture, its ability to define the boundaries while tolerating high deformations makes it another viable choice for simulation of CS multi-particle impact [11,19,21,22]. However, in both cases, the application of SPH for multi-particle/material models requires further modifications to its current implementation in ABAQUS. Furthermore, the absence of a continuous physical boundary, dictates additional post-processing for definition and extraction of interfacial inputs and outputs, respectively.

The Lagrangian and ALE approaches require a lower computation time, and if parameters such as remeshing rule and frequency are selected carefully, the ALE may lead to lower computational costs. The higher computational cost of CEL can be associated with higher element number and larger model scale. SPH stands somewhere between pure Lagrangian and CEL models in terms of computational costs. However, it should be noted that SPH models can be very restrictive regarding parallel computation scalability, which increases their computation time even further. Symmetry in geometry, loading, and boundary conditions of a model can be employed in FEA to reduce the size of the analysis domain and hence, drastically decrease the computation cost and time. However, with SPH method, a full representation of the model is always required; furthermore, SPH is not able to consider the thermal aspects of the CS process [29]. Application of a purely axisymmetric model is only possible using a 2D Lagrangian or ALE model. However, it should be noted that 3D models generally provide more accurate results, besides better visual representation of deformation state.

There are also limitations regarding modeling bonding and adhesion between the incoming particle and the already deposited

ones/the substrate. The materials that are modeled in Eulerian domain, e.g., the particles in a CEL model, exhibit a sticky behavior when impacting each other. Hence, it is impractical to define an inter-particle adhesion law in a CEL model [11,12,20,25,30]. Likewise, when two bodies are discretized using SPH formulation, they cannot separate after contacting each other because of the so-called “pinball” effect. These restrictions make the Lagrangian and ALE models the most convenient ones for establishing a precise adhesion model.

In summary, a comparison was made between the capabilities of Lagrangian, CEL, and SPH as the three most notable FEA approaches based on their capability to.

- a) simulate deformation realistically,
- b) manage the mesh distortion,
- c) exploit the existing symmetries to decrease computation time and cost,
- d) simulate multi-particle impacts,
- e) easily and accurately extract desired outputs, and,
- f) consider aspects necessary for simulation of selective adhesion.

Drawing from authors' experience and the remarks present in the literature [9,13,31–33] the most capable FEA approaches for inspection of each aspect were selected and employed.

Radar diagram presented in Fig. 1 demonstrate a qualitative comparison between the three discussed FEA approaches. Lagrangian, CEL, and SPH approaches are compared and sorted based on their capability to address the requirements listed above.

Supremacy of the Lagrangian approach over the other two in modeling adhesion, possibility of exploiting symmetry to speed up the analysis, and access to accurate output without any post-processing makes it the prominent choice for simulation of the single particle impact. Meanwhile, CEL approach has a higher capability in realistic simulation of the deformation, managing the distortion, and simulating multiple impacts in the same analysis. These characteristics are necessary for a robust and practicable model of multi-particle impact.

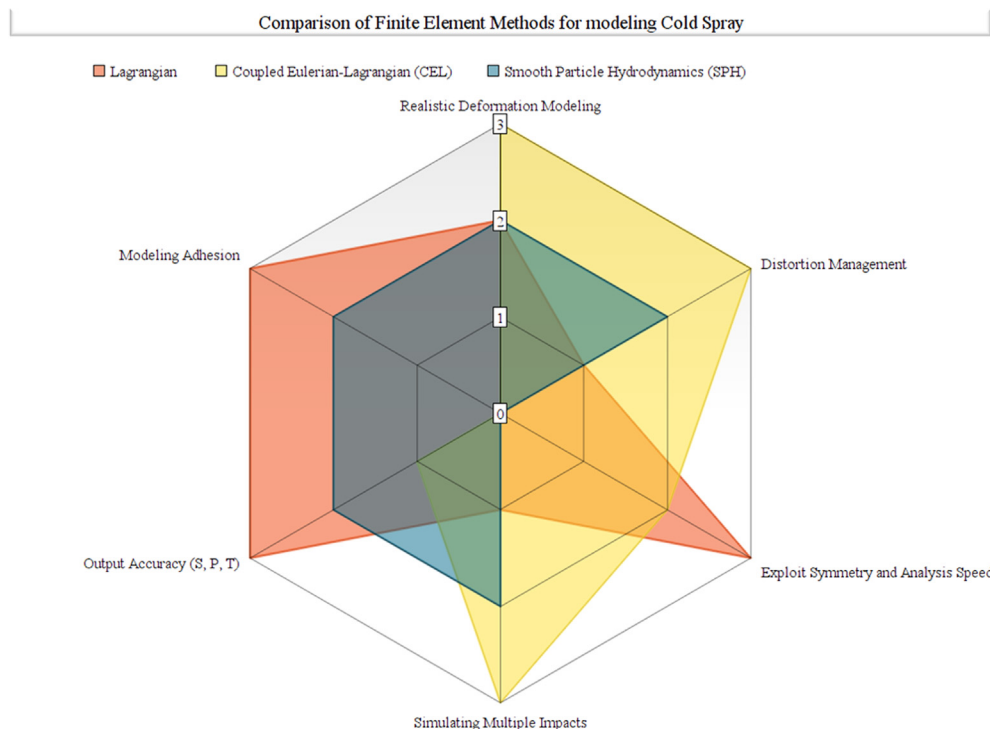


Fig. 1. A qualitative comparison between the capabilities of Lagrangian, CEL, and SPH numerical simulation approaches.

3. Finite element model development

Based on the above comparison and considering the importance of implementing the adhesion feature, Lagrangian and CEL models were developed here and selectively used for evaluating the effect of different powder characteristics. SPH approach was excluded due to the inability to provide an identifiable contact interface that is necessary for the definition of adhesion. In this section, first the material model that was used in both approaches is described; then the details of developed Lagrangian single-particle model are discussed, followed by description of the CEL multi-particle model. The models were used to investigate different sets of process parameters. All the FEA analyses in this research are conducted using Abaqus FEA (Dassault Systemes) [34].

3.1. Material model

Pure aluminum was considered as the constituent material for both substrate and particle. To describe the elastic response, Mie-Grüneisen equation of state and shear modulus were used. Mie-Grüneisen equation of state assumes that the pressure is a linear function of internal energy, but a non-linear function of density as expressed in Eq. (1), assuming a Hugoniot compressive reference curve [35]:

$$p - p_H = \Gamma_\rho (E_m - E_H) \quad (1)$$

where p_H and E_H are the Hugoniot pressure and specific energy (per unit mass), respectively; these parameters are only functions of density, and Γ is the Grüneisen ratio. By substituting the definition of Grüneisen ratio and the relation between Hugoniot pressure and energy, Eq. (2) can be derived:

$$p = p_H \left(1 - \frac{\Gamma_0 \eta}{2} \right) + \Gamma_0 \rho_0 E_m \quad (2)$$

where Γ_0 is a material constant, ρ_0 is the reference density, and $\eta = 1 - \rho_0/\rho$ is the nominal volumetric compressive strain. Eqs. (1) and (2) are the coupled equations for pressure and internal energy, solved at each material point.

Johnson-Cook (JC) plasticity model, which considers the effect of strain, strain rate and temperature, was used as the constituent plasticity model. It expresses the flow stress ($\bar{\sigma}$) as shown in Eq. (3):

$$\bar{\sigma} = \left[A + B \left(\bar{\epsilon}^{pl} \right)^n \right] \left[1 + C \ln \left(\frac{\dot{\bar{\epsilon}}^{pl}}{\dot{\epsilon}_0} \right) \right] \left(1 - \hat{T}^m \right) \quad (3)$$

with \hat{T} being a dimensionless temperature defined in Eq. (4):

$$\hat{T} = f(x) = \begin{cases} 0, & T < T_t \\ \frac{T - T_t}{T_m - T_t}, & T_t < T < T_m \\ 1, & T_m < T \end{cases} \quad (4)$$

In Eqs. (3) and (4), $\bar{\epsilon}^{pl}$ is the equivalent plastic strain, $\dot{\bar{\epsilon}}^{pl}$ is the equivalent plastic strain rate, $\dot{\epsilon}_0$ is the reference plastic strain rate, T_m is the melting temperature of the material, and T_t is the transition temperature, below which yield stress does not depend on temperature. The five remaining coefficients in Eq. (3) are known as JC plasticity coefficients of the material. Coefficient A represents the initial yield strength at room temperature and the reference strain rate, B is the hardening modulus, C is the strain rate sensitivity coefficient, n is the hardening coefficient, and m is the thermal softening coefficient. Temperature-independent properties for elastic and plastic models of pure aluminum are presented in

Table 1

Thermo-mechanical parameters of pure Al at 298° K [36].

Property	Value
Density (T/mm ³)	2.71 E-90
Young's Modulus (MPa)	68,900
Poisson's ratio	0.33
Shear Modulus (MPa)	2.48 E + 04
Mie-Grüneisen EoS constants	CO (mm/s)
	s
	1.339
	Γ_0
	1.97
Johnson-Cook plasticity parameters	A (MPa)
	148.4
	B (MPa)
	345.5
	C
	0.001
	n
	0.183
	m
	0.895
	$T_{melting}$
	916
	$T_{transition}$
	293
	$\dot{\epsilon}_0$ (1/s)
	1
Thermal Conductivity (mW/mm.K)	237.9
Specific Heat (N.mm/T. K)	904 E + 6

Table 1 [36], while temperature-dependent properties, all extracted from MPDB software (Version 8.87, JAHM software Inc.), are presented in the Appendix, Table S1.

3.2. Lagrangian model

3.2.1. Model description

Single-particle impact simulations are useful to provide insight on the effect of various feedstock parameters while avoiding the computational costs of multi-particle models and the interaction between the incoming and deposited particles [37–40]. Here we exploited the existing symmetry, modelling only a quarter of a, unless specified otherwise, perfectly spherical particle with a diameter equal to 40 μm and a cubic substrate with each edge having a length equal to 6 times the particle diameter. As shown in Fig. 2(a), the substrate was partitioned to separate the central impact region of a 100 μm cube for finer meshing. Both parts were discretized into 8 nodes, reduced integration, and combined hour-glass hexahedral structured elements, designated as C3D8R elements. Global mesh size was set equal to 10 μm . However, for the particle and central section of the substrate a finer mesh size equal to 1/25th of the particle radius was applied, which also satisfied the mesh convergence analysis. The particle's axis of symmetry was aligned with the edge of the substrate, and an initial gap of 1 μm was considered between the particle and substrate surface. In all cases, the bottom surface of the substrate was fully fixed, and appropriate symmetry boundary conditions were applied to the side planes for both substrate and the particle.

A series of predefined fields were applied to indicate the initial velocity and temperature. The magnitude and angle of particle velocity for each analysis is indicated in their respective section. Particle and substrate were always assumed to have an initial temperature of 293 K.

3.2.2. Contact and bonding interactions

Adhesion mechanism in CS, while not yet fully established, is generally associated with two phenomena, namely adiabatic shear instability [2] and mechanical interlocking [41]. Both mechanisms are proposed to explain the window of particle velocity in which successful deposition occurs for a given set of materials and process parameters. Thus, adhesion should be implemented in FEA simulation of CS in a way to correlate to and identify the deposition window. At particle velocities lower than the critical velocity (lower threshold for deposition), the particle should rebound and not bond to the substrate surface, while at velocities higher than the other extreme of the window, the model should allow for par-

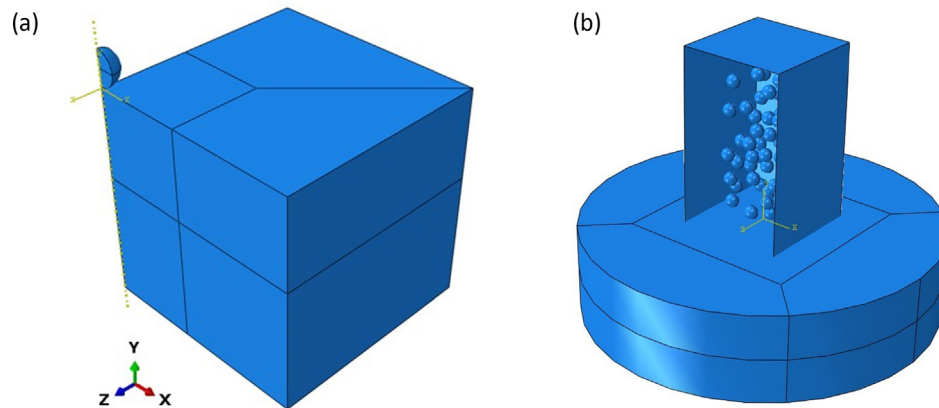


Fig. 2. (a) Single impact Lagrangian model with reflection symmetry, (b) CEL model with randomly positioned multiple particles (one face of the Eulerian domain is removed for better visualization).

particle separation and debonding, accounting for the erosion phenomenon.

The lower band i.e., the critical velocity is the onset of occurrence of jetting and adiabatic shear instability. This leads to a particle expansion large enough to break the oxide layer and expose pristine metallic surfaces of the particle. The fresh metallic surface will adhere to that of the substrate and if the contact area is large enough, the adhesion will be sufficiently strong to avoid particle rebound and will result in successful deposition. Hence, as also suggested by Rahmati et al. [39], the model should be able to distinguish the regions of the particle surface that participate in the adhesion occurrence. To identify the elements on the particle surface that are eligible for adhesion, a two-step approach was implemented here. First, a preliminary analysis was conducted accounting for the shear damage properties of the material. The overall scalar stiffness degradation (SDEG) value [29] was extracted for all the surface elements of the particle, to identify the elements with SDEG values higher than a predefined threshold, here set as 0.02 as recommended for Al in [42]. This value indicates the occurrence of sufficient particle deformation to result in fracture of the outer oxide layer [39]. A general contact, which assumed hard normal behavior with a friction coefficient of 0.3 for the tangential behavior, was defined between the particle and substrate during this preliminary analysis [12,17]. This contact model considered 90 % of the friction's dissipated energy to be converted into heat and did not account for cohesive interaction. The analysis duration for this first step was set as the required time for the system's kinetic energy to reach almost zero (in this case 50 ns). Fig. 3 demonstrates the deformed state and SDEG contour for particles with three impact velocities of 500, 700, and 1000 m/s. Grey regions indicate the surface of the elements that

experience an SDEG higher than 0.02 threshold and hence are assumed to participate in particle–substrate adhesion. Here the expansion of adhesion area with increase of impact velocity is discernible.

The material parameter for shear fracture curve of pure Al was assumed to be $K_s = 0.3$ [42]. The damage evolution parameters of pure Al are presented in Table 2. As mentioned before, shear failure model was implemented to describe the material's behavior under damage. Since the specific shear damage parameters could not be found for pure Al, the parameters extracted for Al7108 alloy were employed [42].

Subsequently, using an ad-hoc python code, the SDEG values of particle's surface elements were extracted and compared against the criterion to identify the individual elements with a high enough SDEG. The code proceeded to create a new model, identical to the initial one, but this time not including the damage model and instead, assigning a cohesive interaction with the substrate to the surface of the identified elements. To model the adhesion, a linear elastic cohesive rule based on Dugdale-Barenblatt law was considered to simulate the traction-separation and the onset of interface failure [38]. In addition, we integrated a damage evolution law to describe the degradation of cohesive stiffness. This approach makes it possible to model the particle rebound at velocities on the higher limit of the deposition window. The result of the second part of the analysis determines whether the CS parameters can lead to a successful deposition or not. Two types of procedures including Dynamic-Explicit and Dynamic/Temperature-displacement Explicit, were considered for the steps. Similar results and considerably lower computation time of the Dynamic-Explicit step led to its selection for both steps in the Lagrangian model.

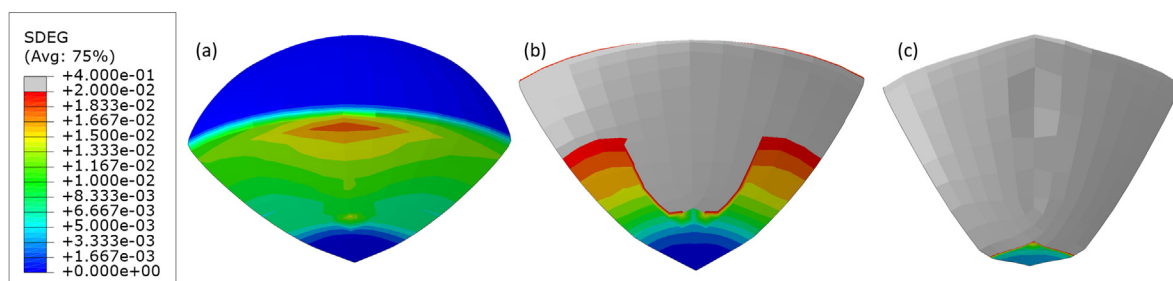


Fig. 3. Damage distribution on particle surface for particle velocities of (a) 500 m/s, (b) 700 m/s, and (c) 1000 m/s. Grey region indicates the elements with SDEG > 0.02 that are eligible for shear instability and thus contribute to adhesion.

Table 2
Damage parameters used for Aluminum [42].

Strain rate	Fracture strain			Shear stress ratio θ_s
	0.0001	0.001	250	
	0.2761	0.2761	0.33382	-10
	0.2761	0.2761	0.33382	14.236
	0.2613	0.2613	0.33361	14.625
	0.253	0.253	0.33552	15.013
	0.251	0.251	0.33955	15.401
	0.2551	0.2551	0.34572	15.789
	0.2656	0.2656	0.35409	16.177
	0.2825	0.2825	0.36473	16.566
	0.3065	0.3065	0.37765	16.954
	0.3379	0.3379	0.39297	17.342
	0.3778	0.3778	0.41077	1.773
	0.4269	0.4269	0.43117	18.118
	0.4865	0.4865	0.4543	18.506
	0.5581	0.5581	0.48038	18.895
	0.6435	0.6435	0.50943	19.283
	0.7448	0.7448	0.54171	19.671
	0.8644	0.8644	0.57742	20.059
	10.053	10.053	0.61678	20.447
	1.171	1.171	0.66005	20.835
	13.655	13.655	0.70762	21.224
	15.937	15.937	0.75956	21.612
	18.611	18.611	0.8163	2.2
	18.611	18.611	0.8163	10

3.3. Coupled Eulerian-Lagrangian model

3.3.1. Model description

The substrate was modeled as a cylindrical Lagrangian domain of 800 μm diameter and 200 μm height. Unless mentioned otherwise, the particles were defined as 30 μm diameter spheres that traveled through a $240 \times 240 \times 425 \mu\text{m}^3$ cuboid, as the Eulerian domain. The bottom section of the Eulerian domain had a partial overlap with the substrate to contain the particle materials during the impact and the depression of the substrate surface.

The model was constructed using a python code. The code started by creating and positioning the Eulerian domain and the substrate. Then particles were created iteratively and positioned in a random location (x_i, y_i, z_i) inside the Eulerian domain above the substrate. The distance of each particle's center from the domain boundaries and the previously created particles was checked to be higher than twice the particle's diameter. The distance between the particle and the domain boundaries was checked to ensure that no material overflow happened in the Eulerian domain. After confirming the validity of the particle's position, the code automatically filled the particle volume with material. This process was repeated until the desired number of particles, in this case 50, were created (see Fig. 2 (b)).

Due to its longer timespan, necessary to ascertain the impact of all particles, multi-particle impact process cannot be assumed as adiabatic. Hence, here the coupled temperature-displacement explicit procedure was selected as the step type.

The substrate's bottom surface was fully fixed. The global mesh size was set to 10 μm , and the substrate's central section and the Eulerian domain were meshed with a finer element size of 2 μm . The substrate was divided into 8-node, thermally coupled elements with reduced integration and stiffness hourglass control, designated as C3D8RT. The Eulerian domain was meshed with structured EC3D8RT elements, like the substrate but with viscous hourglass control.

Since it is not possible to limit the inter-particle and particle-substrate cohesion in a CEL model, only the general contact with hard normal behavior, friction coefficient of 0.3, and 90 % thermal energy dissipation was considered to define the interaction between the particles and the substrate. To assure the complete

impact and deformation of each particle, a longer duration of about 500 ns is considered for the single constituent step that included the impact of all particles.

4. Assessing the role of particle features

4.1. Particle size

Particle size is a key factor that affects multiple aspects of the process, like particle acceleration, impact velocity and particle temperature [43]. The effect of particle size variation was analyzed using the Lagrangian model, assuming spherical particles of 40 μm , 60 μm , and 70 μm diameter. Vertical impact direction and initial temperatures of 473 K and 293 K were assumed for the particle and the substrate, respectively, and were kept constant for all particle sizes, so that the analysis only determines the effect of particle size variation on the critical velocity. To determine the effect of particle size on critical velocity, particle velocity was increased from 300 m/s considering a step size of 25 m/s, until adhesion occurred. The lower band of particle velocity was set based on some initial analyses, to ascertain that the transition from no adhesion to successful adhesion, and consequently identification of critical velocity, was observable in all cases, even the largest particle diameter.

4.2. Particle morphology

Powder manufacturing techniques dictate the dominant particle morphology, with gas atomization process yielding spherical and ellipsoidal particles, and high-pressure water atomization producing more irregular and angular shapes [44]. Particle morphology is reported to influence the drag coefficient, affecting the impact velocities [45–47]. Experimental studies have indicated an increase in the critical velocity for more irregular particles. Irregular and angular particles have been also reported to induce higher porosity compared to spherical particles sprayed at similar conditions [46,48,49]. The importance of the particle's morphological features necessitates a numerical approach that can fully assess the role of morphological variation on deposit quality.

Herein, given the complexity in parametrizing powder particles' morphology, four representative shapes, as presented in Fig. 4a, were considered, including spherical and ellipsoidal particles representing regular shapes, and dodecahedron and hexahedron geometries embodying irregular morphologies. These morphologies were designed based on experimental characterizations provided in [45–47]. For each morphology, except the spherical one, a range of possible rotations were considered, as shown in Fig. 4b.

First the effects of particle morphology and orientation upon impact on the critical velocity were evaluated using the Lagrangian model of single particle impact. For each morphology, the most distinct representative impact orientations were determined. For each orientation, the particle velocity was gradually increased, starting from 300 m/s with 25 m/s increments, until bonding was achieved. This initial velocity was set based on initial estimations and to cover the adhesion transition phase for all cases.

The CEL multi-particle model was employed for assessing the effect of particle morphology on deposit porosity. First for the spheric morphology and based on the selected Rosin-Rammler size distribution [30], Three distinct initial configurations regarding the position and orientation of the particles were created. For other morphologies, each spherical particle was replaced with one of equivalent orientation and equal volume. In the case of ellipsoidal, dodecahedron and hexahedron morphologies, the minimum inter-particle distance was increased compared to the one implemented for the spherical particles. The original minimum distance between the centers of adjacent particles that was set to be greater than the sum of the respective radiuses, was increased by 50 %, to avoid any potential overlap between the irregular morphologies. Once the particle diameter was assigned and particle was positioned, the corresponding velocity was estimated according to the equations presented in [30] considering the density of the material (2970 $\frac{kg}{m^3}$ for Al), gas temperature (1000 K), the local Mach number, the

molecular mass of the carrier gas (28 g/mol for N_2), its specific heat ratio (1.4 for N_2), the stand-off distance (40 mm), and the static pressure at the entrance of the nozzle (4 MPa). The velocities obtained with the described procedure ranged from 550 to 700 m/s.

In order to create the multi-particle sets for other morphologies, first for each morphology a representative geometry with volume of $3.35E-5 \text{ mm}^3$ was created, which is equal to that of a spherical particle with 40 μm diameter. Subsequently, for each specific sphere in a given coordinate, the new morphology was created by scaling all dimensions of the representative geometry up or down to achieve a volume equal to that of the spherical placeholder. This way, in the same set for different morphologies, all particles at the same coordinates, have the same volume, making the analysis results comparable. After simulating the multi-particle impact, porosity was evaluated by means of the output parameter "EVF_VOID", which assumes fractional values ranging from 0 (element filled with material) to 1 (empty element), indicating the porosity of that element. To do so, the biggest parallelepiped that could be completely embedded in the deposit in all cases was selected as the volume control. The EVF_VOID for all the elements enclosed in the volume control was added together, and the ratio of the total void volume to the total volume of the parallelepiped was calculated as the average porosity of the deposit [28]. The average porosities were reported for each particle morphology.

In addition, the effect of morphology was analyzed on flattening ratio, as an index of the particle velocity regime [50]. To this aim, the Lagrangian single-particle model was employed, considering a constant particle velocity of 650 m/s. For spherical particles, the flattening ratio (ε), was defined as in Eq. (5):

$$\varepsilon = \frac{D}{h} \tag{5}$$

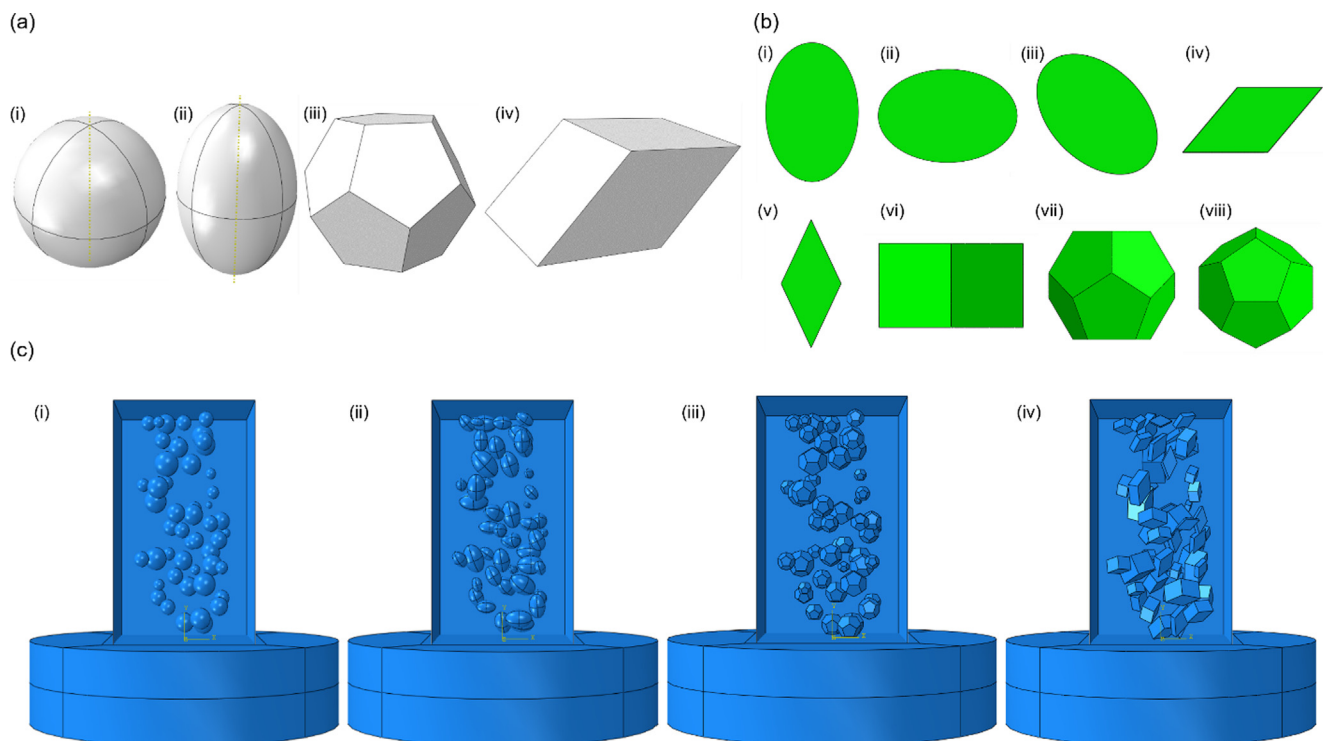


Fig. 4. (a) Representative particle morphologies (i) spherical (ii) ellipsoidal (iii) dodecahedron, and (iv) hexahedron (b) impact orientations considered for each morphology; for ellipsoid: (i) long axis vertical (ii) long axis horizontal and (iii) long axis tilted at 45°, for hexahedron: (iv) rectangular face (v) edge (vi) rhomboidal face, for dodecahedron: (vii) face (viii) vertex; (c) A similar CEL multi-particle configurations for the four distinct particle morphologies considering random dimensions, impact positions and orientations.

where D and h are the particle's initial diameter and the height of the deformed splat, respectively. A higher ε value indicates a more significant particle flattening. While this definition can be easily applied for spherical particles, it proves challenging when irregular shapes with tilted impact orientations are considered, due to the complexity of defining reference geometrical parameters that would be coherently comparable between various particle morphologies. Thus, the following new definition is proposed, hereafter referred to as deformation ratio (DR). For any given morphology, the mid vertical cross section was extracted and the horizontal axis passing through the centroid of this cross section (u axis) was identified. Then the 2nd moment of inertia of the cross section about u -axis (I_{uu}) was calculated for both deformed and undeformed geometries.

$$I_{uu} = \int_A r^2 dA \quad (6)$$

in which A refers to the area of central cross section of the particle, and r is the vertical distance of the integration increment dA from the horizontal u -axis, as visualized in Fig. 5.

Then using Eq. (7), an equivalent radius was estimated for both the undeformed ($R_{eq,i}$) and deformed ($R_{eq,f}$) geometries. Finally, the deformation ratio was expressed as the ratio between the initial and the final equivalent radii of the particle's mid cross section (Eq. (8)). With this definition, a higher DR indicates higher particle deformation.

$$R_{eq} = \sqrt{\frac{I_{uu}}{A}} \quad (7)$$

$$DR = \frac{R_{eq,i}}{R_{eq,f}} \quad (8)$$

4.3. Particle's outer oxide layer

Metallic materials involved in the CS process, commonly have a high affinity to oxygen, which makes the presence of surface oxide layer unavoidable. As Assadi et al. [51] suggest, the contact of newly exposed metallic surfaces between the particle and substrate is essential for bonding in CS. This is achieved by disrupting the naturally formed oxide layer and its ejection from the contact area. Therefore, not only the oxide layer confines the exposed contact area, but also a portion of particle's kinetic energy should be dedicated to *in-situ* disruption of the oxide layer, leaving less energy for adhesion, and thus lowering the probability of deposition. The effect of reduced energy can also be inferred from the lower flattening ratio of the particles with a thicker oxide layer [52].

The single particle Lagrangian model was modified to analyze the effect of the presence and the thickness of oxide layer on critical velocity. To capture the brittle behavior of the oxide layer, as suggested by Kim et al. [53] and Petrackova [48], the Johnson-Holmquist (JH) material model was considered for the oxide layer

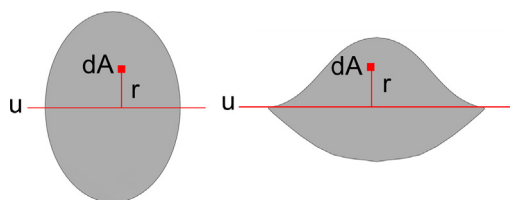


Fig. 5. Schematic showing the mid cross section used for the calculation of the 2nd moment of inertia in the case of a representative undeformed (left) and deformed (right) particle.

material. The JH model is suitable for modelling brittle materials, which undergo large strains at high strain rates. It considers the progressive increase in the damage variable with plastic deformation. Since Aluminum was the selected particle material, oxide layer was assumed to be made of Alumina, for which the JH-2 constants are presented in the Appendix, Table S2. The particle its surrounding oxide layer were created as separate parts, and then assembled using a tie constraint. The oxide layer was divided into smaller ($0.6 \mu\text{m}$) elements to ensure the presence of at least 2 elements across the oxide layer thickness. Particle velocity was gradually increased, starting from 300 m/s at increments of 25 m/s. The results were strongly dependent on the oxide layer thickness. Hence, the values reported in the literature for particle diameter (D) and oxide layer thickness (t) were gathered and categorized based on the t/D ratio as shown in Table S3, to allow for a systematic choice of layer thickness as a function of the selected particle diameter [48,52–57]. Considering the average ratio of 0.00335 obtained from experimental data and the average ratio of 0.014729 obtained by averaging all the available experimental and numerical data and multiplying them by the representative particle diameter of $40 \mu\text{m}$, three oxide layer thicknesses equal to 0.1, 0.2 and $0.3 \mu\text{m}$ were modelled to evaluate the effect of oxide layer on critical velocity.

4.4. Particle's impact angle

Studying the effect of angle of impact is of particular importance both for repair and additive manufacturing when dealing with an irregular substrate, or a complex geometry for which it is not possible to consider the deposition at 90° . Thus, ascertaining how the coating properties change according to the spraying angle can lead to an optimized spraying strategy. The impact direction of each particle may differ from 90° based on the flow characteristics or the orientation of the nozzle with respect to the substrate. The angle of impact indicates the angle between the direction of the particle's trajectory and the normal of substrate surface at the point of impact. It can affect the particle deformation, and consequently the deposit characteristics such as deposition efficiency and thickness, porosity, and its adhesion strength [58].

The single impact Lagrangian model was used to evaluate the critical velocity for different impact angles, considering that when assessing the impact angles of 30° and 60° , symmetry could not be exploited. In each case, the particle velocity was gradually increased from 500 to 900 m/s with 100 m/s intervals, while monitoring the bonding of the particle to the substrate.

Another set of analyses were conducted to study the effect of impact angle on deposit porosity using the multi-particle CEL model. Three different impact angles of 60° , 75° , and 90° were imposed by tilting the Eulerian domain about Z-axis and assigning appropriate components of initial velocities to the particles, as shown in Fig. 6. Three configurations each with a distinct particle arrangement were analyzed per impact angle. The Eulerian domain size was further increased to avoid material outflow. Deposit porosity was evaluated in a $100 \times 100 \times 20 \mu\text{m}^3$ parallelepiped, which is the biggest one that could be completely fitted in the deposit in all 3 cases, as depicted in Fig. 6d, following the procedure developed in our previous study [28].

5. Results and discussion

5.1. The effects of feedstock characteristics on critical velocity

5.1.1. Particle size

Regarding the particle size, the Lagrangian model was able to successfully predict the onset of particle bonding and deposition,

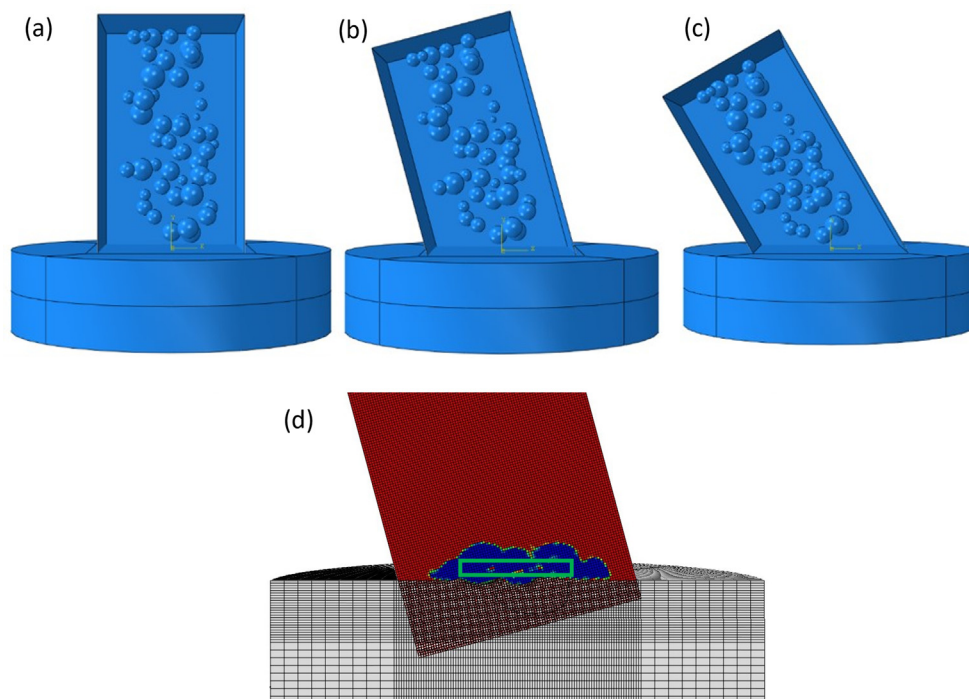


Fig. 6. (a)-(c) set of CEL models used to evaluate the effect of angle of impact on porosity, d) the volume control considered for calculation of porosity.

hence determine the critical velocity for each diameter. Increasing the particle diameter resulted in an approximately linear reduction of the critical velocity, as reported in Table 3, which is in agreement with the trends reported in the literature [57]. As summarized in Table 3, the estimated critical velocity for Al particles of 40 μm diameter were lower than the experimentally measured values reported in an study [60], while another experimental study that covers a wider range of Al particle sizes shows more comparable results with our estimations [59]. However, it is important to highlight that the diameter is not the only variable that affects the critical velocity; besides the substrate properties, surface state and temperature, and the particle size can also define its temperature and affect the thickness of the oxide layer as well. The important aspect to underline is that the model correctly predicts the trend of the critical velocity as a function of diameter variation.

Fig. 7 demonstrates the distribution of plastic equivalent strain (PEEQ) and the state of adhesion after impact for two particles with diameters of 60 μm and 70 μm at similar particle velocity of 400 m/s. As can be seen in Fig. 7, the lower kinetic energy (affected by the higher mass) of the 60 μm particle induces plastic deformation at smaller magnitude and distribution, while the impact of 70 μm particle results in a considerable plastic deformation and successful adhesion. In conclusion, as the particle's size (in this case, the spherical particle's diameter) increases, the minimum velocity required for inducing bonding with the substrate decreases.

In conclusion, as the particle's size (in this case, the spherical particle's diameter) increases, its critical velocity decreases.

5.1.2. Particle morphology

Considering the effect of particle morphology, despite the relatively regular form of the ellipsoidal particle, the variation of impact orientation still affected its critical velocity. The impact configuration with vertical long axis exhibited the lowest critical velocity and the horizontal long axis impact showed the highest critical velocity, as reported in Table 4. Fig. 8 represents the deformation for vertical, horizontal, and tilted impact of ellipsoidal particle at two different velocities. The more severe deformation after vertical impact can explain the lower critical velocity for this configuration. The critical velocity identified for the particle tilted to 45° is between the two other extremes.

For the particles with dodecahedron shape, the difference between the critical velocities associated with the two considered orientations, was much less, compared to the variations noticed for the ellipsoidal form. This is because while in dodecahedron shape the sharp edges induce irregularity, the difference between its principal dimensions is much less compared to the ellipsoidal shape. On the contrary, changing the impact orientation of hexahedron particle resulted in significant variation in the estimated critical velocity.

Fig. 9 illustrates the distribution of plastic equivalent strain at the interface for impact of four representative morphologies at 600 m/s. Despite higher irregularity of dodecahedron and hexahedron morphologies, the effect of impact orientation and contact area has led to their successful deposition, while the ellipsoid has rebounded from the substrate surface.

Table 3

Effect of particle diameter: comparison of the numerically estimated critical velocities with experimental data reported for Al spherical particles.

Particle diameter (μm)	40	60	70	Experimental data	
				40 [60]	65 [59]
Critical velocity [m/s]	525	425	400	750	440

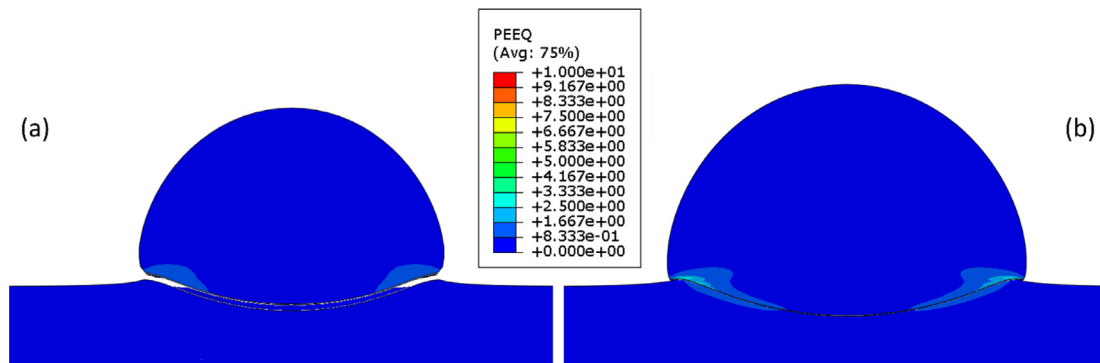


Fig. 7. PEEQ distribution and the state of adhesion of particles with diameters of a) 60 μm and b) 70 μm both flying at velocity of 400 m/s.

Table 4

The effect of particle morphology: critical velocities estimated for regular and irregular morphologies as a function of impact orientation.

Particle shape	Sphere	Ellipsoid	Dodecahedron		Hexahedron		
Particle impact orientation							
Estimated critical velocity (m/s)	525	425	625	575	575	625	400
Average critical velocity per particle shape (m/s)	525	542	592	600	600	600	800

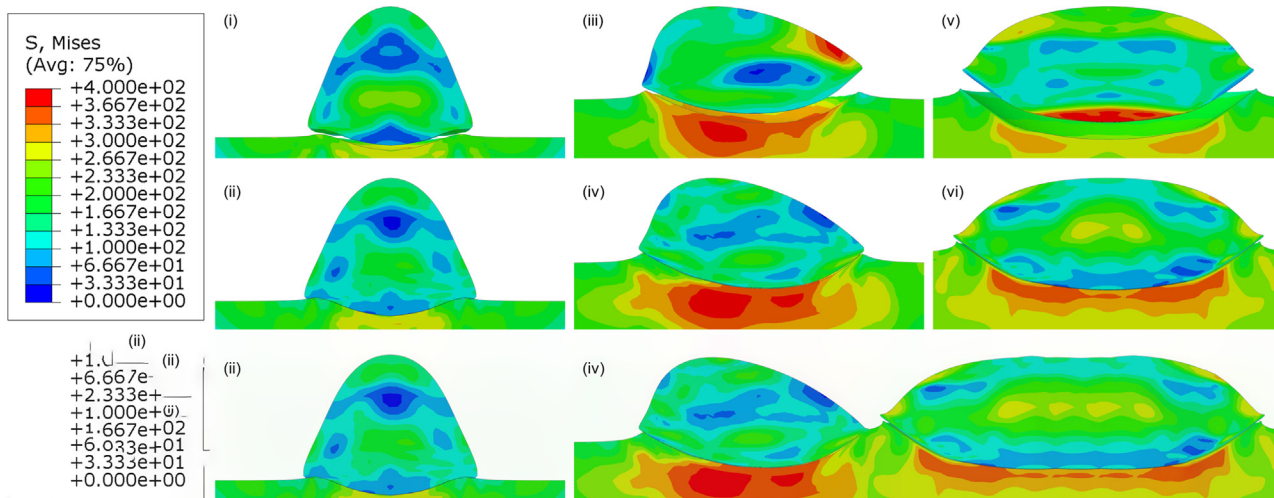


Fig. 8. von-Mises contours representing the effect of particle morphology: deformation contours for ellipsoidal particle impacting with different orientations: (i and ii) long axis vertical impacting at 400 m/s and 425 m/s; (iii and iv) Long axis tilted at 45° at 550 m/s and 575 m/s; (v and vi) long axis vertical at 600 m/s and 625 m/s.

While the effect of orientation on critical velocity is evident, the averaged values reported in Table 4 confirm that, overall, higher morphological irregularity will result in a higher critical velocity.

Comparison of the average critical velocities between the regular (spherical and ellipsoidal) and the irregular (dodecahedron and hexahedron) morphologies reveals a difference of around 60 m/s that is close to 10 % of the corresponding absolute value. This trend is in line with the results of experimental studies [45,46] reporting that passing from spherical to irregular particles, the critical velocity increases. As an example, Ning et al. estimated the critical velocity for copper feedstock of dense-spherical and irregular particle morphologies [45]. They estimated the critical velocity through combination of cumulative in-flight particle velocity distribution and deposition efficiency of the different feedstocks and reported critical velocities of 425 and 550 m/s for spherical and irregular particle morphologies, respectively. This increase in crit-

ical velocity for the more irregular morphologies, matches the trend present in numerical results of our finite element model.

It should be noted that in CS, the stream of pressurized gas, which flows through the de Laval nozzle, provides acceleration to the powder particles through drag forces that in turn rely on the aerodynamic interactions. So, for a given set of CS parameters, higher irregularity will induce larger drag coefficient implying higher acceleration and thus higher flight speed. But in this study the influence of the shape on the flight speed is not addressed and we have imposed the flight speed in the model with the aim to estimate the corresponding critical velocity.

In conclusion, it is notable that for asymmetric morphologies, various factors such as general orientation, interfacial contact area, and the angle of impact affect the state of adhesion. However, considering the average critical velocity, as a more conclusive index that represents the general state of particle impact during CS, the

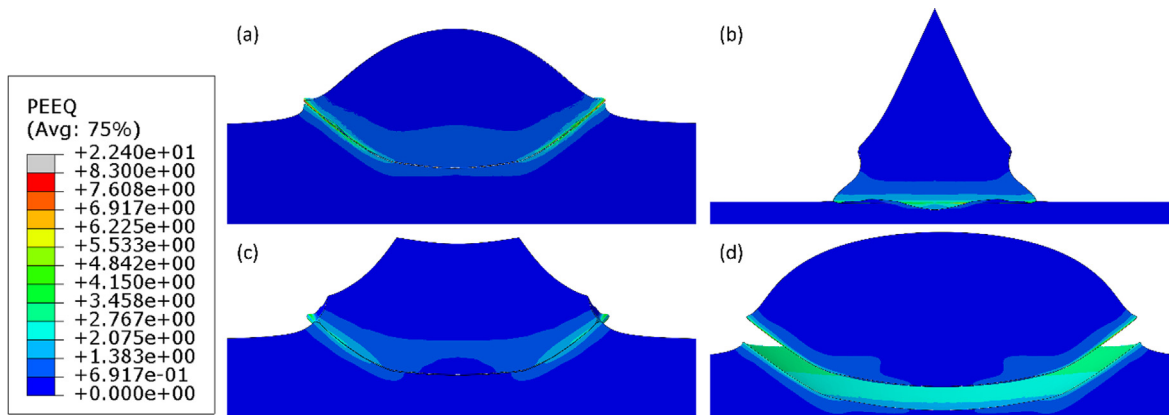


Fig. 9. PEEQ contours for impact of four representative geometries at 600 m/s, with the maximum PEEQ reported for each geometry as follows: a) sphere: 25.3, b) hexahedron: 22.4, c) dodecahedron: 9.57, d) ellipsoid: 8.29.

results confirmed that higher irregularity of the particle morphology will result in a higher critical velocity.

5.1.3. Oxide layer

The presence of the oxide layer can affect the deposition kinetics, thus different simulations were performed to evaluate the effect of the oxide layer on critical velocity, qualitatively and quantitatively. Fig. 10 shows the damage parameter contour within the oxide layer at the impact instance for particles with outer oxide layers of different thicknesses at two velocities: just under and equal to the critical velocity. The constitutive model used to describe the oxide layer's brittle behavior provided a good description of the layer's failure during the impact. In all cases, a sufficiently high velocity resulted in disruption and ejection of most of the oxide layer on the bottom surface of the particle, promoting intimate contact of freshly

exposed metallic surfaces. When considering an oxide layer of 0.1 μm around a 40 μm diameter particle, the critical velocity was estimated to be 550 m/s, which is higher than the velocity needed for the adhesion of the same particle without any oxide layer (i.e., 525 m/s). At this velocity, the whole oxide layer at the bottom part of the particle was removed, therefore promoting metallurgical bonding. As presented in Table 5, the simulations indicate that having a thicker oxide layer increases the corresponding critical velocity, adversely affecting the deposition, as confirmed in experimental studies [52,56,61]. Studies have also shown that the remaining oxide layer at the interface can limit the adhesion strength and reduce the extent of bonded surface [52,54].

Kang et al. [52] created four Al feedstocks with artificially controlled oxygen content increasing, and in each case measured and reported the critical velocity, as presented in Table 6.

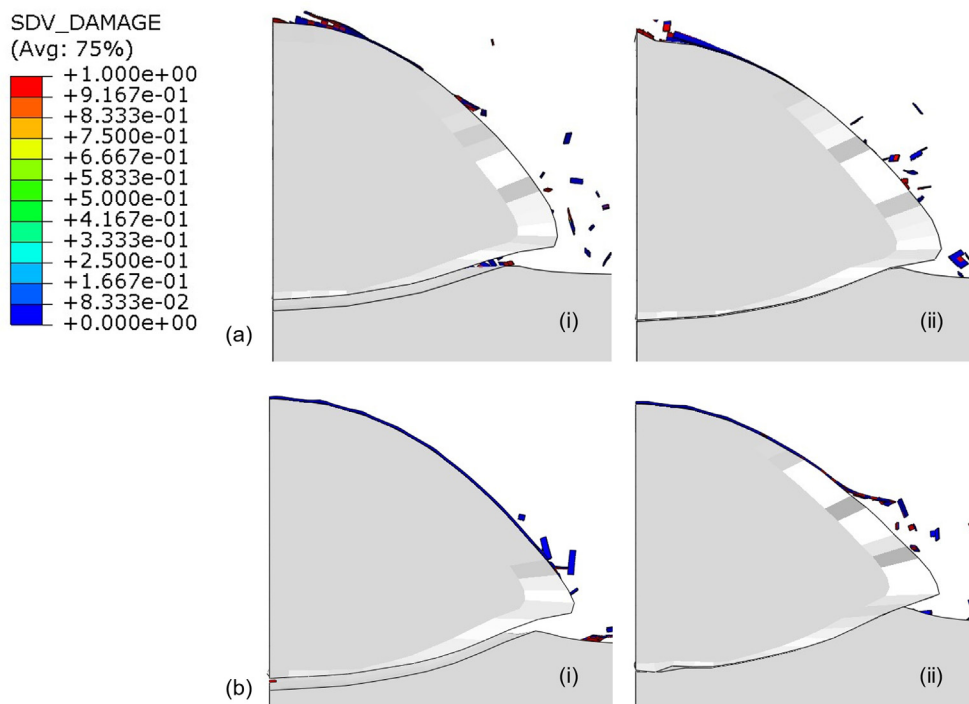


Fig. 10. The effect of oxide layer thickness: the impact instance of a particle with oxide layer of (a) 0.1 μm thickness: (i) 525 m/s (ii) 550 m/s and (b) 0.2 μm thickness: (i) 575 m/s (ii) 600 m/s.

Table 5

The effect of oxide layer thickness on critical velocity.

Oxide layer thickness (μm)	0	0.1	0.2	0.3
Critical speed (m/s)	525	550	600	650

Table 6

Variation of critical velocity of Al particles with the oxygen content [52].

Oxygen content (% wt)	0.001	0.012	0.023	0.045
Critical speed (m/s)	721	742	808	867

The linear increase in critical velocity of particles with higher oxidation [52] is in agreement with the numerical results of the presented FEA model.

5.1.4. Angle of impact

Regarding the effect of angle of impact on critical velocity, representative results for impact angle of 60° are shown in Fig. 11, estimating the lower band of critical velocity to be 600 m/s. However, at 600 m/s, only a small bonding region is observed, making the particle susceptible to break loose when hit by an upcoming particle. This would justify the decrease in the deposition efficiency (DE) and thickness of the coating reported in [62–64] for deposition of Cu on Steel with impact angles of 90° to 30° , Al on Al 2024 T-3 with impact angles of 90° to 30° , and Ti on Al-Cu-SS with impact angles of 90° to 60° , respectively. At higher velocities the splat's resting position was extended but gradually moved towards outside of the induced crater. For 900 m/s instead, the asymmetry of the deformation is more notably accentuated, with a large portion of the particle laying outside of the crater. Therefore, the stability of bonding is lower, making the adhesion even weaker. 900 m/s could be estimated as the higher band for the deposition window, above which adhesion may be easily broken after the impact. At lower impact angles of 45° , bonding occurred at 700 and the higher end of deposition window was identified at 900 m/s within a very small adhesion zone; while, at the impact angle of 30° , bonding was never strong enough to avoid the sliding and rebound of the deformed particle (see Fig. 12).

Hence, it can be concluded that for a similar combination of feedstock and process parameters, which implies a constant in-flight velocity for a specific particle, a decrease in impact angle means higher required critical velocity and weaker adhesion, i.e., lower probability of particle's successful deposition, and lower overall deposition efficiency.

Experimental studies have confirmed that deviating from normal impact direction can decrease the DE [7], which can be expressed as the ratio of the weight of the powder bonded to the substrate to the total weight of the sprayed powder; For Al and Cu particles threshold for getting zero DE was reported to be between 30° and 50° and it was reported that below 50° the majority of the particles were rebounded [62,63]. It should be noted that as explained before, the particle size also affects the deposition efficiency and critical velocity. However, in general optimum deposition angle has been experimentally proved to be 90° leading to better bonding and lower porosity [62–64].

Fig. 13 presents a comparison between the observed cross-section and the FEA results for particle impact at 60° and 45° at a velocity of 700 m/s. The experiments were conducted for a feedstock of Al 6061 spherical powders with an average particle diameter equal to $40 \mu\text{m}$, equal to that considered in this study. It is discernable that the FEA model can accurately predict the variation of particle deformation, as well as position and extension of the jetting region and the particle–substrate interface gap for different angles of impact [7].

5.2. The effects of feedstock characteristics on porosity

Feedstock properties play a major role in defining the porosity of the deposit. For instance, particle morphology affects the porosity through changing the in-flight velocity and the extent of deformation. Here, the CEL multi-impact model was employed to estimate the effect of particle morphology on porosity. The results presented in Table 7 indicate that per each morphology, different arrangements and particle impact orientations do not result in a significant porosity variation. The ellipsoidal and spherical particles led to a similar average porosity, while a lower scatter was observed in the case of spherical powders. On the other hand,

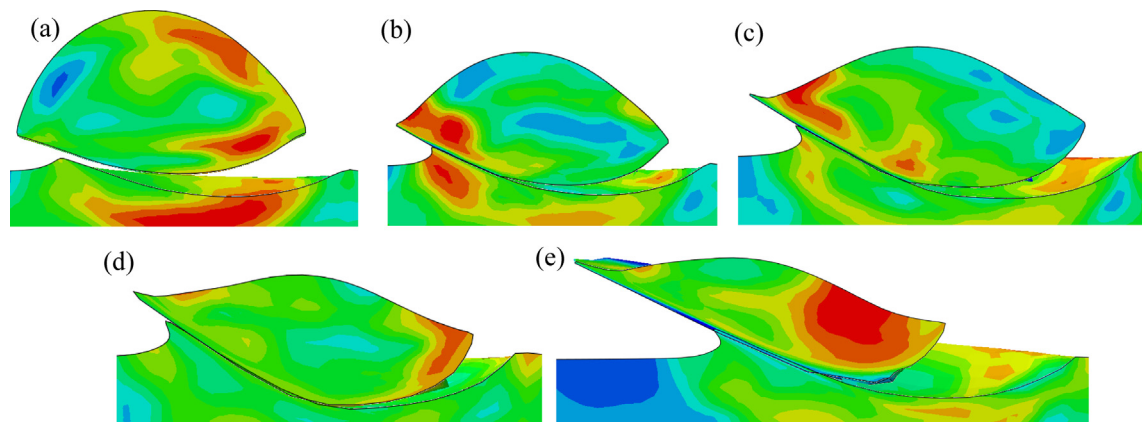


Fig. 11. von-Mises contours representing the effect of angle of impact: sectioned view of single particle model, with impact angle of 60° at different velocities of (a) 500 m/s (b) 600 m/s (c) 700 m/s (d) 800 m/s and (e) 900 m/s.

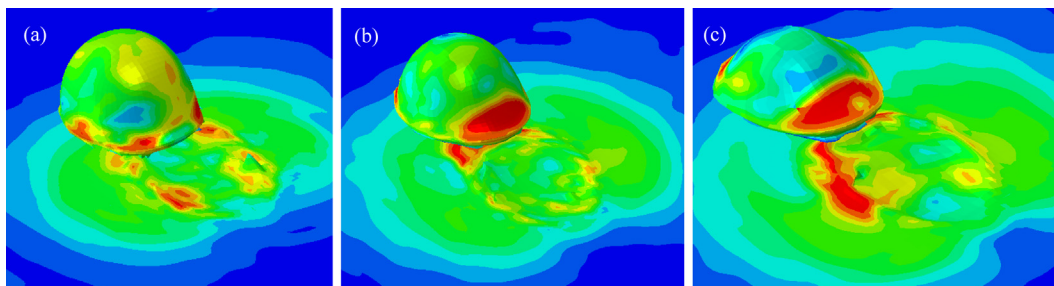


Fig. 12. von-Mises contours representing the effect of angle of impact: single particle model with impact angle of 30° at different velocities of (a) 600 m/s (b) 700 m/s and (c) 900 m/s.

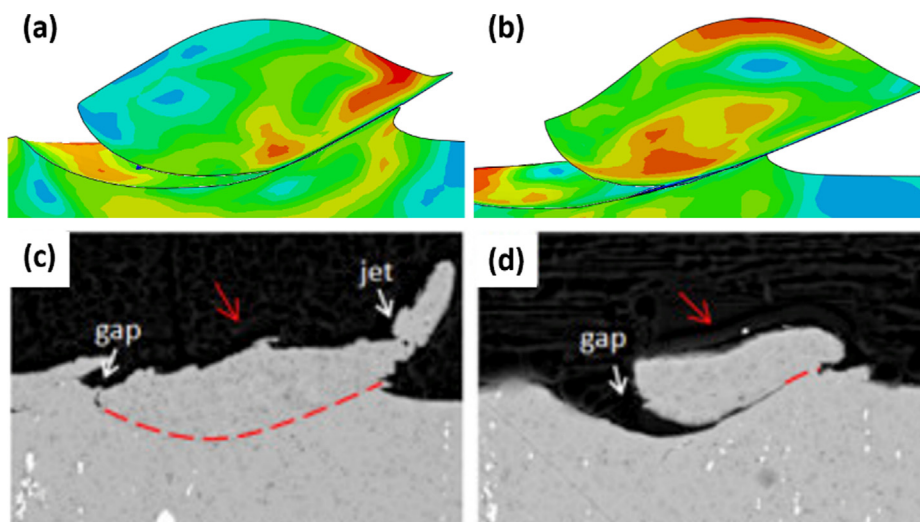


Fig. 13. A comparison between FEA results of this study and the experimental observations [7] for evolution of 40 μm Al particle's deformation, jetting region, and interfacial gap for impact angles of (a, c) 60°, and (b, d) 45°.

Table 7
The effect of particle morphology on porosity estimated for the three configurations per particle shape (each set has a different particle arrangement).

Particle morphology	Porosity set 1	Porosity set 2	Porosity set 3	Average porosity
Spherical	2.95 %	3.12 %	3.06 %	3.04 %±0.0862
Ellipsoidal	3.06 %	2.76 %	3.20 %	3.01 %±0.2227
Dodecahedron	3.93 %	4.11 %	4.27 %	4.10 %±0.1701
Hexahedron	5.29 %	5.34 %	4.97 %	5.20 %±0.2007

the dodecahedron and hexahedron particles led to a higher porosity, compared to the regular morphologies, with the hexahedron shape showing the highest porosity. The hexahedron geometry can be considered similar to the morphology referred to as angular in experimental studies [65,66]. These works corroborate the same trend observed between the irregularity of the particle and the porosity of the CS deposits [46,49,65–67], confirming that the spherical particles induce a lower porosity compared to the irregular or angular ones [46,66].

To evaluate the effect of particle impact angle (60°, 75°, and 90°) on porosity, for each angle three particle arrangements including the spherical particles' positioning, dimension, and velocity were created considering P = 4 MPa, T = 1000 K [30]. Porosity values measured in a representative horizontal parallelepiped volume fitted inside the deposit, are presented in Table 8. The results show an increase in porosity as the impact angle decreases. Within the same set, the arrangement of the particles changes the porosity value around 0.2 %. The results indicate that the rate of porosity increase is much higher at lower angles. The obtained trend agrees

with what reported in [58]. The results of this study showed a notable difference in porosity between when setting 90° (<0.2 %) and 45° (>6.5 %) for angle of impacts. The reported trend was not linear but increased exponentially from 90° to 45°. Yin et al. [64] also reported a similar non-linear trend when depositing irregular Ti particles on copper, aluminium, and stainless steel (SS) substrates at spraying angles of 90°, 75°, 60°. Moreover, Petrackova et al. [68] showed that an impact angle close to 90° resulted in low porosity, while porosity increased by deviating from normal orientation.



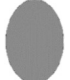






5.3. The effects of feedstock characteristics on flattening ratio

The Lagrangian model was used to simulate single impacts for different morphologies and orientations all flying at the constant velocity of 650 m/s. The calculated deformation ratios together with visual representation of particle orientation are reported in Table 9.

Table 8
The effect of particle impact angle on porosity for the three configurations per orientation (Each set has a different particle arrangement).

Angle of impact	Porosity set 1	Porosity set 2	Porosity set 3	Average porosity
90°	2.95 %	3.12 %	3.06 %	3.04 %±0.0862
75°	3.73 %	3.82 %	3.89 %	3.81 %±0.0802
60°	6.53 %	6.38 %	6.65 %	6.52 %±0.1353

Table 9
Effect of morphology and orientations on DR.

Shape/orientation	DR	Average DR per shape category	Visual representation
Sphere	1.54	1.54	
Ellipsoidal / short axis vertical	1.48	1.59 ± 0.099	
Ellipsoidal / long axis vertical	1.63		
Ellipsoidal / tilted at 45°	1.66		
Dodecahedron / vertex	1.62	1.80 ± 0.251	
Dodecahedron / face	1.97		
Hexahedron / rectangular face	1.65	1.72 ± 0.060	
Hexahedron / rhomboidal face	1.70		
Hexahedron /edge	1.80		

The results show a considerable variation of DR between different morphologies. A comparison between the average values, to account for the impact orientation variations, can help distinguish the effect of morphology, while drawing attention to the highest variation that was measured for the dodecahedron shape, showing a high scatter of 20 %. The regular shapes (spherical and ellipsoid) show similar DR range that is lower than those calculated for the angular shapes (dodecahedron and hexahedron). However, it should be noted that it is difficult to experimentally identify the effect of the particle morphology on the deformation ratio, given that normally irregular particles have a higher drag coefficient and therefore different impact velocities.

Regarding the influence of the oxide layer, experimental studies have confirmed the role of oxide layer in reducing the extent of deformation, although in some cases not significant [48,52,55]. The few numerical studies [53,55] based on adaptive mesh formulation have confirmed a lower deformation and compression ratio (defined as the ratio of height variation to the initial diameter) for higher oxide thickness. This trend can be attributed to the portion of the energy dissipated for breaking the oxide layer, thus decreasing the available energy for particle deformation. Kim et al. [53] also highlighted that, the maximum temperature in the particle with oxide layer was lower compared to that of the oxide-free particle. This can affect the thermal softening, with a consequent decrease in deformation state.

6. Conclusions

This study offers a holistic numerical framework able to predict the influence of various feedstock characteristics on multiple mechanical and physical aspects of the cold spray deposit. The results evidenced that given the complexity of the cold spray deposition process due to the severe and high-rate plastic deformation of the particles upon impact, it is not possible to define a universal numerical model to analyse the effect of all parameters. Three major simulation strategies of Lagrangian, coupled Eulerian Lagrangian (CEL) and smoothed particle hydrodynamics (SPH) were compared in terms of advantages and disadvantages for cold spray modelling. Lagrangian and CEL techniques were developed and validated through comparison with experimental data available in the literature. The models were used to investigate the effect of individual feedstock parameters including particle dimension, morphology, oxide layer thickness and angle of impact on major quality indexes such as critical velocity, particle flattening and deposit porosity. The most suitable numerical modelling strategy was identified and used to analyse the correlation between each pair of parameters.

Critical velocity was extracted thanks to the bonding model developed based on shear damage and instability in the interaction zone. The model provided a good estimation of critical velocity and window of deposition as a function of different powder characteristics. The critical velocity was found to decrease with an increase

in the particle size. Assuming a similar in-flight velocity and neglecting the larger drag coefficient of the irregular particles, the particles were divided in two geometrical classes of regular (sphere and ellipsoid) and irregular (dodecahedron and hexahedron) to analyse the effect of morphology on critical velocity. The critical velocity of the irregular particles was estimated to be higher than the regular ones. The presence of the oxide layer was confirmed to be detrimental for critical velocity. The higher the thickness of the oxide layer, the higher the velocity required to achieve adhesion. This will lead to reduced deposition efficiency; thus, obtaining a desired deposit thickness will require longer deposition times or a higher gas pressure in the presence of thick oxide layer. In both cases, the cost of the process will be dramatically increased. Inclined deposition angles narrowed the range of velocity at which adhesion occurred. For deposition angles smaller than 45°, adhesion never happened, regardless the particle velocity. The results indicate that the spraying angle of 90° should be prioritized where possible, given that it allows to achieve a good deposition efficiency with lowest porosity. The models offer the possibility of estimating the critical orientation angle for each deposition condition, that will be useful both for repair and additive manufacturing applications.

In terms of porosity, the optimal spraying angle was found to be 90°. The results showed that the impacts inclined at 75° led to a relatively small increase (around 20 % with respect to the normal impact) in porosity, while further tilting to 60° doubled the porosity compared to normal spraying. The use of spherical or ellipsoidal particles caused lower porosity, compared to the irregular shapes. Thus, the results promote the use of the more regular particles due to their higher deposition efficiency and lower porosity.

A new deformation index was suggested to analyse the flattening behaviour of different morphologies. Irregular particles exhibited higher deformation ratios compared to the spherical and ellipsoidal particles, when flying at same velocities. Thus, the simulations can identify the effect of the morphology on particle flat-

tening, without considering of the higher speed of the irregular particles at the same spray conditions, due to their larger drag coefficient. Deformation ratio was decreased as the thickness of the oxide layer increased.

Overall, the developed framework provides the possibility of performing a systematic study on the deposit characteristics, eliminating the need for the costly and time-consuming experimental tests required for their optimization. The developed models offer guidelines for selection and optimization of cold spray deposition parameters

Data availability

Data will be made available on request.

Declaration of Competing Interest

The authors declare that they have no known competing financial interests or personal relationships that could have appeared to influence the work reported in this paper.

Acknowledgement

The research leading to these results has received funding from the European Union’s Horizon 2020 research and innovation programme under grant agreement No 101004172 (ATLAS, Advanced Design of High Entropy Alloys Based Materials for Space Propulsion).

Appendix

Table S1
Temperature-dependent properties of Aluminum.

Temperature (K)	Density (Tonne/mm ³)	Temperature (K)	Shear Modulus, G, (MPa)	Temperature (K)	Thermal Conductivity (mW/mm.K)	Temperature (K)	Specific Heat (N.mm/Tonne.K)
20	2.7340E-09	0	2.8947E + 04	0	0.0000E + 00	100	4.8166E + 08
50	2.7337E-09	30	2.8885E + 04	30	4.8951E + 03	130	6.0903E + 08
80	2.7323E-09	60	2.8723E + 04	60	7.8583E + 02	160	7.0358E + 08
110	2.7293E-09	90	2.8483E + 04	90	3.2384E + 02	190	7.7251E + 08
140	2.7255E-09	120	2.8184E + 04	120	2.6898E + 02	220	8.2213E + 08
170	2.7212E-09	150	2.7842E + 04	150	2.4587E + 02	250	8.5782E + 08
200	2.7165E-09	180	2.7472E + 04	180	2.3883E + 02	280	8.8410E + 08
230	2.7114E-09	210	2.7084E + 04	210	2.3731E + 02	310	9.0457E + 08
260	2.7062E-09	240	2.6687E + 04	240	2.3592E + 02	340	9.2203E + 08
290	2.7007E-09	270	2.6288E + 04	270	2.3443E + 02	370	9.3812E + 08
320	2.6951E-09	300	2.5889E + 04	300	2.3720E + 02	400	9.5309E + 08
350	2.6893E-09	330	2.5491E + 04	330	2.3915E + 02	430	9.6715E + 08
380	2.6835E-09	360	2.5093E + 04	360	2.3999E + 02	460	9.8051E + 08
410	2.6775E-09	390	2.4691E + 04	390	2.4000E + 02	490	9.9339E + 08
440	2.6715E-09	420	2.4276E + 04	420	2.3941E + 02	520	1.0060E + 09
470	2.6653E-09	450	2.3840E + 04	450	2.3842E + 02	550	1.0185E + 09
500	2.6590E-09	480	2.3370E + 04	480	2.3715E + 02	580	1.0312E + 09
530	2.6527E-09	510	2.2851E + 04	510	2.3571E + 02	610	1.0442E + 09
560	2.6461E-09	540	2.2265E + 04	540	2.3416E + 02	640	1.0578E + 09
590	2.6395E-09	570	2.1593E + 04	570	2.3254E + 02	670	1.0722E + 09
620	2.6326E-09	600	2.0812E + 04	600	2.3086E + 02	700	1.0876E + 09
650	2.6256E-09	630	1.9895E + 04	630	2.2912E + 02	730	1.1042E + 09
680	2.6184E-09	660	1.8816E + 04	660	2.2731E + 02	760	1.1221E + 09
710	2.6111E-09	690	1.7543E + 04	690	2.2541E + 02	790	1.1418E + 09
740	2.6036E-09	720	1.6043E + 04	720	2.2341E + 02	820	1.1632E + 09
770	2.5959E-09	750	1.4280E + 04	750	2.2130E + 02	850	1.1867E + 09
800	2.5881E-09	773	1.2727E + 04	780	2.1908E + 02	880	1.2124E + 09

(continued on next page)

Table S1 (continued)

Temperature (K)	Density (Tonne/mm ³)	Temperature (K)	Shear Modulus, G, (MPa)	Temperature (K)	Thermal Conductivity (mW/mm.K)	Temperature (K)	Specific Heat (N.mm/Tonne.K)
830	2.5802E-09			810	2.1678E + 02	910	1.2407E + 09
860	2.5723E-09			840	2.1445E + 02	933	1.2641E + 09
890	2.5645E-09			870	2.1217E + 02		
920	2.5568E-09			900	2.1004E + 02		
933	2.5535E-09			930	2.0824E + 02		
				933	2.0809E + 02		

Table S2

JH-2 Parameters for Alumina [69].

Density	ρ_0 (Tonne/mm ³)	3.89E-9
Shear Modulus	G (MPa)	152,000
Hugoniot elastic limit	HEL (MPa)	7000
Intact strength constant	A	0.88
Intact strength constant	N	0.64
Strain rate constant	C	0.007
Fracture strength constant	B	0.45
Fracture strength constant	M	0.60
Max strength of failed material/HEL stress	SFMAX	1.0
Tensile strength	T (MPa)	462
Pressure (EOS) constant 1	K ₁ (MPa)	231,000
Pressure (EOS) constant 2	K ₂ (MPa)	-160000
Pressure (EOS) constant 3	K ₃ (MPa)	2,774,000
Bulking constant	BULK	1
Damage constant 1	D ₁	0.0125
Damage constant 2	D ₂	0.70

Table S3

List of particle size and the correspondent experimentally measured oxide layer thicknesses.

Thickness [μm]	Particle diameter [μm]	Ratio t/D	Comments	Reference paper
0.02	10	0.002	Experimental	[54]
0.15	65	0.002308	Experimental	[52]
0.4	20	0.02	Numerical	[55]
0.8	20	0.04	Numerical	[55]
0.1	65	0.001538	Both	[53]
0.2	65	0.003077	Both	[53]
0.3	65	0.004615	Both	[53]
0.35	37	0.009459	Experimental	[57]
0.2	28	0.007143	Numerical	[44]
2	28	0.071429	Numerical	[44]
0.005	11	0.000455	Experimental	[56]

References

- [1] A. Papyrin, V. Kosarev, S. Klinkov, A. Alkhimov, V.M. Fomin, Cold Spray Technology, 2007. <https://doi.org/10.1016/B978-0-08-045155-8.X5000-5>.
- [2] H. Assadi, F. Gärtner, T. Stoltenhoff, H. Kreye, Bonding mechanism in cold gas spraying, Acta Mater. 51 (2003) 4379–4394. [https://doi.org/10.1016/S1359-6454\(03\)00274-X](https://doi.org/10.1016/S1359-6454(03)00274-X).
- [3] S. Bagherifard, M. Guagliano, Fatigue performance of cold spray deposits: Coating, repair and additive manufacturing cases, Int. J. Fatigue. 139 (2020). <https://doi.org/10.1016/j.ijfatigue.2020.105744> 105744.
- [4] S. Bagherifard, S. Monti, M.V. Zuccoli, M. Riccio, J. Kondás, M. Guagliano, Cold spray deposition for additive manufacturing of freeform structural components compared to selective laser melting, Mater. Sci. Eng. A. 721 (2018) 339–350. <https://doi.org/10.1016/j.msea.2018.02.094>.
- [5] S. Yin, P. Cavaliere, B. Aldwell, R. Jenkins, H.L. Manufacturing, undefined 2018, Cold spray additive manufacturing and repair: Fundamentals and applications, Elsevier. (n.d.). <https://www.sciencedirect.com/science/article/pii/S2214860417302993> (accessed April 12, 2021).
- [6] S. Bagherifard, J. Kondas, S. Monti, J. Cizek, F. Perego, O. Kovarik, F. Lukac, F. Gaertner, M. Guagliano, Tailoring cold spray additive manufacturing of steel 316 L for static and cyclic load-bearing applications, Mater. Des. 203 (2021). <https://doi.org/10.1016/j.matdes.2021.109575> 109575.
- [7] X. Wang, F. Feng, M.A. Klecka, M.D. Mordasky, J.K. Garofano, T. El-Wardany, A. Nardi, V.K. Champagne, Characterization and modeling of the bonding process in cold spray additive manufacturing, Addit. Manuf. 8 (2015) 149–162. <https://doi.org/10.1016/j.addma.2015.03.006>.
- [8] J. Vlcek, L. Gimeno, H. Huber, E. Lugscheider, A systematic approach to material eligibility for the cold-spray process, J. Therm. Spray Technol. 14 (2005) 125–133. <https://doi.org/10.1361/10599630522738>.
- [9] R. Ghelichi, S. Bagherifard, M. Guagliano, M. Verani, Numerical simulation of cold spray coating, Surf. Coatings Technol. 205 (2011) 5294–5301. <https://doi.org/10.1016/j.surfcoat.2011.05.038>.
- [10] X. Song, J. Everaerts, W. Zhai, H. Zheng, A.W.Y. Tan, W. Sun, F. Li, I. Marinescu, E. Liu, A.M. Korsunsky, Residual stresses in single particle splot of metal cold spray process – Numerical simulation and direct measurement, Mater. Lett. 230 (2018) 152–156. <https://doi.org/10.1016/j.matlet.2018.07.117>.
- [11] S. Yin, X.F. Wang, B.P. Xu, W.Y. Li, Examination on the calculation method for modeling the multi-particle impact process in cold spraying, J. Therm. Spray Technol. 19 (2010) 1032–1041. <https://doi.org/10.1007/s11666-010-9489-9>.
- [12] J. Xie, D. Nélías, H.W. Le Berre, K. Ogawa, Y. Ichikawa, Simulation of the cold spray particle deposition process, J. Tribol. 137 (2015) 1–15. <https://doi.org/10.1115/1.4030257>.
- [13] W.Y. Li, C. Zhang, C.J. Li, H. Liao, Modeling aspects of high velocity impact of particles in cold spraying by explicit finite element analysis, J. Therm. Spray Technol. 18 (2009) 921–933. <https://doi.org/10.1007/s11666-009-9325-2>.

- [14] S. Shah, J. Lee, J.P. Rothstein, Numerical Simulations of the High-Velocity Impact of a Single Polymer Particle During Cold-Spray Deposition, *J. Therm. Spray Technol.* 26 (2017) 970–984, <https://doi.org/10.1007/s11666-017-0557-2>.
- [15] M.K. Hamiyanze, T.-C. Jen, Numerical Analysis of the Cold Gas Dynamic Spray Surface Coating Process, in: Core.Ac.Uk, Atlantis Press, 2017: pp. 75–79. <https://doi.org/10.2991/icmmse-17.2017.13>
- [16] A. Ardehshiri Lordejani, L. Vitali, M. Guagliano, S. Bagherifard, Estimating deposition efficiency and chemical composition variation along thickness for cold spraying of composite feedstocks, *Surf. Coatings Technol.* 436 (2022), <https://doi.org/10.1016/j.surfcoat.2022.128239> 128239.
- [17] B. Yildirim, S. Muftu, A. Gouldstone, Modeling of high velocity impact of spherical particles, *Wear* 270 (2011) 703–713, <https://doi.org/10.1016/j.wear.2011.02.003>.
- [18] R.A. Gingold, J.J. Monaghan, Smoothed particle hydrodynamics: theory and application to non-spherical stars, *Mon. Not. R. Astron. Soc.* 181 (1977) 375–389, <https://doi.org/10.1093/mnras/181.3.375>.
- [19] B. Gnanasekaran, G.-R. Liu, Y. Fu, G. Wang, W. Niu, T. Lin, A Smoothed Particle Hydrodynamics (SPH) procedure for simulating cold spray process - A study using particles, *Surf. Coatings Technol.* 377 (2019) 124812.
- [20] D. Nélias, J. Xie, H. Walter-Le Berre, Y. Ichikawa, K. Ogawa, Simulation of the Cold Spray Deposition Process for Aluminum and Copper using Lagrangian, ALE and CEL Methods, *Thermomech. Ind. Process. Model. Numer. Simul.* 9781848213 (2014) 321–358, <https://doi.org/10.1002/9781118578759.ch17>.
- [21] Z. Zhang, C. Shu, M.S.U. Khalid, Y. Liu, Z. Yuan, Q. Jiang, W. Liu, SPH modeling and investigation of cold spray additive manufacturing with multi-layer multi-track powders, *J. Manuf. Process.* 84 (2022) 565–586, <https://doi.org/10.1016/j.jmapro.2022.10.032>.
- [22] W.K.W. Tai, R. Chakrabarty, S. Pinches, X. Huang, J. Lang, J. Song, A.S.M. Ang, Comparing Relative Bond Characteristics Between Spherical and Elongated Morphologies for Cold Spray Process Using SPH Simulation, *J. Therm. Spray Technol.* 31 (8) (2022) 2489–2504.
- [23] A.A. Hemedat, C. Zhang, X.Y. Hu, D. Fukuda, D. Cote, I.M. Nault, A. Nardi, V.K. Champagne, Y. Ma, J.W. Palko, Particle-based simulation of cold spray: Influence of oxide layer on impact process, *Addit. Manuf.* 37 (2021), <https://doi.org/10.1016/j.addma.2020.101517> 101517.
- [24] J. Xie, D. Nélias, H. Walter-Le Berre, Y. Ichikawa, K. Ogawa, Numerical simulation of the cold spray deposition process for aluminum and copper, *ASME 2012 11th Bienn. Conf. Eng. Syst. Des. Anal. ESDA 2012* (1) (2012) 109–111, <https://doi.org/10.1115/ESDA2012-82107>.
- [25] S. Weiller, F. Delloro, P. Lomonaco, M. Jeandin, C. Garion, A finite elements study on porosity creation mechanisms in cold sprayed coatings, *Key Eng. Mater.* (2019) 358–363, <https://doi.org/10.4028/www.scientific.net/KEM.813.358>.
- [26] X. Song, X.Z. Jin, W. Zhai, A.W.Y. Tan, W. Sun, F. Li, I. Marinescu, E. Liu, Correlation between the macroscopic adhesion strength of cold spray coating and the microscopic single-particle bonding behaviour: Simulation, experiment and prediction, *Appl. Surf. Sci.* 547 (2021), <https://doi.org/10.1016/j.apsusc.2021.149165>.
- [27] A. Fardan, C.C. Berndt, R. Ahmed, Numerical modelling of particle impact and residual stresses in cold sprayed coatings: A review, *Surf. Coatings Technol.* 409 (2021), <https://doi.org/10.1016/j.surfcoat.2021.126835> 126835.
- [28] M. Terrone, A. Ardehshiri Lordejani, J. Kondas, S. Bagherifard, A.A. Lordejani, J. Kondas, S. Bagherifard, A numerical approach to design and develop freestanding porous structures through cold spray multi-material deposition, *Surf. Coatings Technol.* 421 (2021), <https://doi.org/10.1016/j.surfcoat.2021.127423> 127423.
- [29] ABAQUS, ABAQUS Documentation 2018, (2018).
- [30] X. Song, K.L. Ng, J.M.K. Chea, W. Sun, A.W.Y. Tan, W. Zhai, F. Li, I. Marinescu, E. Liu, Coupled Eulerian-Lagrangian (CEL) simulation of multiple particle impact during Metal Cold Spray process for coating porosity prediction, *Surf. Coatings Technol.* 385 (2020), <https://doi.org/10.1016/j.surfcoat.2020.125433> 125433.
- [31] M. Yu, W.Y. Li, F.F. Wang, H.L. Liao, Finite element simulation of impacting behavior of particles in cold spraying by Eulerian approach, *J. Therm. Spray Technol.*, Springer (2012) 745–752, <https://doi.org/10.1007/s11666-011-9717-y>.
- [32] S.T. Oyinbo, T.C. Jen, Investigation of the process parameters and restitution coefficient of ductile materials during cold gas dynamic spray (CGDS) using finite element analysis, *Addit. Manuf.* 31 (2020), <https://doi.org/10.1016/j.addma.2019.100986> 100986.
- [33] R. Chakrabarty, J. Song, Crystal plasticity finite element investigation of deformation of single crystal copper during cold spray, *Addit. Manuf.* 49 (2022), <https://doi.org/10.1016/j.addma.2021.102484> 102484.
- [34] D.S. Simulia, Abaqus/Standard Theory Manual, Version 6.14, Dassault Syst. Simulia Corp. Provid. RI, 2010.
- [35] A.U. Manual, Abaqus user manual, Abacus (2020).
- [36] W.Y. Li, W. Gao, Some aspects on 3D numerical modeling of high velocity impact of particles in cold spraying by explicit finite element analysis, *Appl. Surf. Sci.* 255 (2009) 7878–7892, <https://doi.org/10.1016/j.apsusc.2009.04.135>.
- [37] P. Profizi, Development of a numerical model of single particle impact with adhesion for simulation of the Cold Spray process, 2016. <http://theses.insa-lyon.fr/publication/2016LYSEI088/these.pdf> (accessed June 16, 2021).
- [38] A. Viscusi, Numerical investigations on the rebound phenomena and the bonding mechanisms in cold spray processes, in: AIP Conf. Proc., American Institute of Physics Inc., 2018. <https://doi.org/10.1063/1.5034957>.
- [39] S. Rahmati, B. Jodoin, Physically Based Finite Element Modeling Method to Predict Metallic Bonding in Cold Spray, *J. Therm. Spray Technol.* 29 (2020) 611–629, <https://doi.org/10.1007/s11666-020-01000-1>.
- [40] P. Profizi, A. Combesure, K. Ogawa, SPH modeling of adhesion in fast dynamics: Application to the Cold Spray process, *Comptes Rendus - Mec.* 344 (2016) 211–224, <https://doi.org/10.1016/j.crme.2016.02.001>.
- [41] T. Hussain, D.G. McCartney, P.H. Shipway, D. Zhang, Bonding mechanisms in cold spraying: The contributions of metallurgical and mechanical components, *J. Therm. Spray Technol.* 18 (2009) 364–379, <https://doi.org/10.1007/s11666-009-9298-1>.
- [42] H. Hooputra, H. Gese, H. Dell, H. Werner, A comprehensive failure model for crashworthiness simulation of aluminium extrusions, *Int. J. Crashworthiness.* 9 (2004) 449–464, <https://doi.org/10.1533/jicr.2004.0289>.
- [43] T. Stoltenhoff, H. Kreye, H.J. Richter, An analysis of the cold spray process and its coatings, *J. Therm. Spray Technol.* 11 (2002) 542–550, <https://doi.org/10.1361/105996302770348682>.
- [44] F.J. Brodmann, Cold spray process parameters: powders, in: *Cold Spray Mater. Depos. Process*, Elsevier, 2007: pp. 105–116.
- [45] X.J. Ning, J.H. Jang, H.J. Kim, The effects of powder properties on in-flight particle velocity and deposition process during low pressure cold spray process, *Appl. Surf. Sci.* 253 (2007) 7449–7455, <https://doi.org/10.1016/j.apsusc.2007.03.031>.
- [46] W. Wong, P. Vo, E. Irissou, A.N. Ryabinin, J.-G. Legoux, S. Yue, Effect of Particle Morphology and Size Distribution on Cold-Sprayed Pure Titanium Coatings, *J. Therm. Spray Tech.* 22 (7) (2013) 1140–1153.
- [47] H. Fukanuma, N. Ohno, B. Sun, R. Huang, In-flight particle velocity measurements with DPV-2000 in cold spray, *Surf. Coatings Technol.* 201 (2006) 1935–1941, <https://doi.org/10.1016/j.surfcoat.2006.04.035>.
- [48] K. Petrčáková, From Structural Repairs To Additive Manufacturing - Exploring New Challenges for Cold Spray, 2018. <https://www.politesi.polimi.it/handle/10589/139096> (accessed September 16, 2021).
- [49] Y.J. Li, X.T. Luo, C.J. Li, Dependency of deposition behavior, microstructure and properties of cold sprayed Cu on morphology and porosity of the powder, *Surf. Coatings Technol.* 328 (2017) 304–312, <https://doi.org/10.1016/j.surfcoat.2017.08.070>.
- [50] A.A. Tamiyu, C.A. Schuh, Particle flattening during cold spray: Mechanistic regimes revealed by single particle impact tests, *Surf. Coatings Technol.* 403 (2020), <https://doi.org/10.1016/j.surfcoat.2020.126386> 126386.
- [51] H. Assadi, H. Kreye, F. Gärtner, T. Klassen, Cold spraying - A materials perspective, *Acta Mater.* 116 (2016) 382–407, <https://doi.org/10.1016/j.actamat.2016.06.034>.
- [52] K. Kang, S. Yoon, Y. Ji, C. Lee, Oxidation dependency of critical velocity for aluminum feedstock deposition in kinetic spraying process, *Mater. Sci. Eng. A.* 486 (2008) 300–307, <https://doi.org/10.1016/j.msea.2007.09.010>.
- [53] K.H. Kim, W. Li, X. Guo, Detection of oxygen at the interface and its effect on strain, stress, and temperature at the interface between cold sprayed aluminum and steel substrate, *Appl. Surf. Sci.* 357 (2015) 1720–1726, <https://doi.org/10.1016/j.apsusc.2015.10.022>.
- [54] W.Y. Li, C.J. Li, H. Liao, Significant influence of particle surface oxidation on deposition efficiency, interface microstructure and adhesive strength of cold-sprayed copper coatings, *Appl. Surf. Sci.* 256 (2010) 4953–4958, <https://doi.org/10.1016/j.apsusc.2010.03.008>.
- [55] W.Y. Li, H. Liao, C.J. Li, H.S. Bang, C. Coddet, Numerical simulation of deformation behavior of Al particles impacting on Al substrate and effect of surface oxide films on interfacial bonding in cold spraying, *Appl. Surf. Sci.* 253 (2007) 5084–5091, <https://doi.org/10.1016/j.apsusc.2006.11.020>.
- [56] J. Lienhard, C. Crook, M.Z. Azar, M. Hassani, D.R. Mumm, D. Veyssat, D. Apelian, K.A. Nelson, V. Champagne, A. Nardi, C.A. Schuh, L. Valdevit, Surface oxide and hydroxide effects on aluminum microparticle impact bonding, *Acta Mater.* 197 (2020) 28–39, <https://doi.org/10.1016/j.actamat.2020.07.011>.
- [57] Y. Ichikawa, K. Ogawa, Effect of Substrate Surface Oxide Film Thickness on Deposition Behavior and Deposition Efficiency in the Cold Spray Process, *J. Therm. Spray Technol.* 24 (2015) 1269–1276, <https://doi.org/10.1007/s11666-015-0299-Y>.
- [58] K. Binder, J. Gottschalk, M. Kollenda, F. Gärtner, T. Klassen, Influence of impact angle and gas temperature on mechanical properties of titanium cold spray deposits, in: *J. Therm. Spray Technol.* (2011) 234–242, <https://doi.org/10.1007/s11666-010-9557-1>.
- [59] T.H.V. Steenkiste, J.R. Smith, R.E. Teets, Aluminum coatings via kinetic spray with relatively large powder particles, *Surf. Coatings Technol.* 154 (2002) 237–252, [https://doi.org/10.1016/S0257-8972\(02\)00018-X](https://doi.org/10.1016/S0257-8972(02)00018-X).
- [60] I. Dowding, M. Hassani, Y. Sun, D. Veyssat, K.A. Nelson, C.A. Schuh, Particle size effects in metallic microparticle impact-bonding, *Acta Mater.* 194 (2020) 40–48, <https://doi.org/10.1016/j.actamat.2020.04.044>.
- [61] C.J. Li, W.Y. Li, H. Liao, Examination of the critical velocity for deposition of particles in cold spraying, *J. Therm. Spray Technol.* 15 (2006) 212–222, <https://doi.org/10.1361/105996306X108093>.
- [62] C.J. Li, W.Y. Li, Y.Y. Wang, G.J. Yang, H. Fukanuma, A theoretical model for prediction of deposition efficiency in cold spraying, *Thin Solid Films* 489 (2005) 79–85, <https://doi.org/10.1016/j.tsf.2005.05.002>.
- [63] Q. Blochet, F. Delloro, F. N'Guyen, F. Borit, M. Jeandin, K. Roche, G. Surdon, Influence of spray angle on cold spray with Al for the repair of aircraft components, *Hal.Archives-Ouvertes.Fr.* (2014) 69–74. <https://hal.archives-ouvertes.fr/hal-01055104> (accessed September 7, 2021).
- [64] S. Yin, X. Suo, J. Su, Z. Guo, H. Liao, X. Wang, Effects of substrate hardness and spray angle on the deposition behavior of cold-sprayed Ti particles, *J. Therm.*

- Spray Technol., Springer (2014) 76–83, <https://doi.org/10.1007/s11666-013-0039-0>.
- [65] V.S. Bhattiprolu, K.W. Johnson, O.C. Ozdemir, G.A. Crawford, Influence of feedstock powder and cold spray processing parameters on microstructure and mechanical properties of Ti-6Al-4V cold spray depositions, Surf. Coatings Technol. 335 (2018) 1–12, <https://doi.org/10.1016/j.surfcoat.2017.12.014>.
- [66] J. Tang, Z. Zhao, N. Li, X. Qiu, Y. Shen, X. Cui, H. Du, J. Wang, T. Xiong, Influence of feedstock powder on microstructure and mechanical properties of Ta cold spray depositions, Surf. Coatings Technol. 377 (2019). <https://doi.org/10.1016/j.surfcoat.2019.124903>.
- [67] V.N.V. Munagala, V. Akinyi, P. Vo, R.R. Chromik, Influence of Powder Morphology and Microstructure on the Cold Spray and Mechanical Properties of Ti6Al4V Coatings, J. Therm. Spray Technol. 27 (2018) 827–842, <https://doi.org/10.1007/s11666-018-0729-8>.
- [68] K. Petráčková, J. Kondás, M. Guagliano, Fixing a hole (with cold spray), Int. J. Fatigue. 110 (2018) 144–152, <https://doi.org/10.1016/j.ijfatigue.2018.01.014>.
- [69] A. Tasdemirci, I.W. Hall, Numerical and experimental studies of damage generation in multi-layer composite materials at high strain rates, Int. J. Impact Eng. 34 (2007) 189–204, <https://doi.org/10.1016/j.ijimpeng.2005.08.010>.